Noninvasive Conductivity and Temperature Sensing using Magnetic Induction Spectroscopy Imaging

Imamul Muttakin, *Member, IEEE,* Manuchehr Soleimani

***Abstract*—The work presents a perspective in evaluating electromagnetic tomography reconstruction through a spectral eddy current imaging arrangement. Embarking from an established analytical basis, the spectroscopic relation of a metallic conductive body to its physical properties is revealed via multi-frequency mutual impedance measurement. Characteristics are evident, from either modelling or experiment, on certain frequency ranges that discriminate the object's circumstances. Both the amplitude ratio and phase-contrast image spectrum show information on the conductivity and structure of a target considered pivotal for industrial applications. Two test cases are reported: liquid metal structure determination, and contactless temperature evaluation of a remote/hidden medium/object. Using eddy current based spectroscopic imaging data and appropriate calibration, this work for a first time demonstrates a novel thermal mapping system. This is a wireless and inductive based temperature mapping device that can have great potential applications where none of the existing thermal measuring devices could work noninvasive.**

***Index Terms*—mutual impedance, spectral imaging, conductive material, temperature measurement, magnetic induction tomography.**

I. Introduction

INDUSTRIAL sectors demand decisive information for supervision, quality assessment, as well as regulating a process. Inductive measurement has several desirable advantages, such as remote sensing technique, non-intrusive, sturdy operation, etc. In addition, multiple frequencies data contain important characteristics of the measurand, particularly a conductive body. Distinctive patterns are known for conductivity level and target's size [1], [2]. As a consequence, this instance has inspired various implementations.

The spectrum of electromagnetic induction was applied for identification of buried conductive and/or permeable landmines independent on the depth or orientation. Therefore, the identification is only based on spectral shapes where the object's signature can be obtained [3], [4]. The recent implementation of magnetic spectroscopy for mine detection was also proposed in [5]. Furthermore, the method was referred for classifying non-ferrous metal waste to be recovered based on its purity [6]. On the other hand, inversion of induction spectroscopy measurement into conductivity distribution image form was among interesting research. The work disclosed in [7] offers an ability to extract depth and internal profile of the target.

In the continuous steel casting, it is desirable to observe the flowing liquid metal content inside pouring nozzle [8]. It has an important –but yet to be quantified– role for flow pattern, hence the quality, further down in the mould to end product. Multi-frequency inductive measurement could provide an identification necessary to determine non-conductive distribution embedded in conductive steel jet. The presence of gas bubbles (deliberately injected to prevent clogging and remove impurities) disrupts the induced eddy current more profoundly in higher frequency. The test reported in [9] correlated a frequency crossover point that discriminates between annular and bubbly liquid metal flow. This peculiar feature has not been exploited further to distinguish different flow regimes.

Correspondingly, the observation of temperature profile of hot steel inside the billet has been attempted. Internal map of electrical conductivity which is related to the measurement of the solid, mushy and liquid layers was reported [10]. The study synchronises the magnetic induction tomography (MIT) and the thermal map from the actual process parameters. This paves prospective research on temperature reconstruction based on conductivity detection through magnetic induction. Moreover, the possibility will enhance the development and application of temperature measurement technologies [11].

The response of conductive objects toward magnetic field excitation over different frequencies is picked up as induction spectroscopy data. This work makes use of those facts to propose tomographic images based on electromagnetic induction and illustrate them in spectroscopic fashion exposing electrical properties and physical circumstances of a target for further interpretation. Spectral imaging can provide useful features to leverage more advance practices.

II. Method

The ratio of absolute mutual impedance (presence of conductive object against air background) plots a sigmoid shape along the frequency to converge at an asymptote; whereas phase change curves down to an extreme point before bouncing back towards zero as frequency increases. The straightforward explanation is associated with skin-depth phenomena, that is the eddy currents tend to buoy towards the surface and ultimately stick there at a higher frequency. Consequently, the response field is invariant to the object's conductivity (penetration depth is negligible) and staying in-phase with the excitation field.

Modelling in COMSOL is utilised to solve electromagnetic field problem of coil combinations [12], and simulated to preliminarily confirm the aforementioned. A pair of coils (solenoid) are modelled as the exciter-detector arranged opposite (axial distance 15 mm) to each other. A cylinder sample

I. Muttakin and M. Soleimani are with the Department of Electronic & Electrical Engineering, University of Bath, Claverton Down, BA2 7AY, United Kingdom e-mail: (see researchportal.bath.ac.uk/en/persons/imamul-muttakin).

Manuscript received April 19, 2005; revised August 26, 2015.

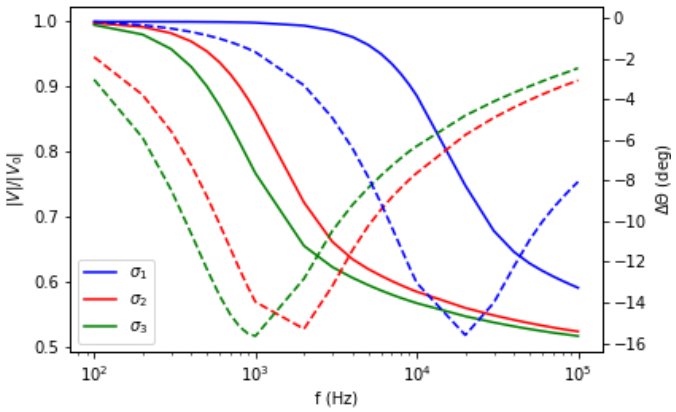

Fig. 1: Behaviour of Conductive Body as Function of Induced Voltage and Frequency. Amplitude (—) and phase (- -); conductivity σ_1 (blue) = $0.1\sigma_2$ (red) = $0.05\sigma_3$ (green).

(diameter 7.5 mm) is placed in between coils, in such a way that the cylinder's axis is perpendicular to the coils' axis. The exciter coil is injected by a unit ac current in frequency sweep mode (100 Hz – 100 kHz), and the induced voltage at the detector coil is recorded for each frequency. The reference voltage (V_0) is the induced voltage when the measurement is taken without the conductive sample (air background); whereas V is induced with the presence of the sample. Fig. 1 shows amplitude (left y-axis, solid line plot) and phase (right y-axis, dashed line plot) of induced voltage when the cylinder object's conductivity is varied (σ_1 = 3 MS/s, σ_2 = 30 MS/s, and σ_3 = 60 MS/s) relative to air (σ_0 = 0).

A. Mutual Impedance in Two-Coil System

The method based on mutual impedance measurement between transmitting coil (excited by a current source) and receiving coil (from which induced voltage is sensed). Having established reference measurement with air background condition, the relationship between induced voltage V and excitation current I is,

$$V = j\omega M I \tag{1}$$

where M is mutual inductance between transmitter and receiver coils.

When an object with electromagnetic properties is placed in between coils, the spatial distribution of the magnetic field is perturbed. Consequently, the change in mutual inductance ΔM raises a modification in the detection signal ΔV at receiving coil, re-arranged into:

$$\Delta M = \frac{\Delta V}{j\omega I} \tag{2}$$

Here, the current is kept at an independent level. ΔM is a complex value consists of resistive and reactive components. Magnetic material will increase the mutual induction between coils, hence increasing the measured signal; whereas conductive material will reduce the signal. In other words, the real part of the impedance change represents a change in the magnetic flux while the imaginary part represents the loss due to the eddy currents.

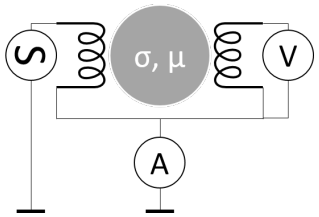

Fig. 2: Mutual Impedance Measurement Scheme.

As depicted in Fig. 2, pair of transmitter and receiver coils (2200R, Murata Power Solutions, L = 220 μH) are arranged to face each other (separating distance of 20 mm, with effective sensing space of 15 mm) in which an object will be placed midway between them. The transmitting coil is excited by a current source to generate a magnetic field that will be picked up by the receiving coil. The induced voltage at terminals of receiving coil can be sensed as a function of the primary field from the transmitter as well as a secondary field depends on any perturbation exists in the sensing area. Eddy currents will occur on conductive samples from which some information about the object in question are carried by the secondary field relative to the primary field.

In the experiments, the transmitter coil is injected with 10 mA source in frequency-sweep procedure; while the receiver coil is being sensed by measuring bridge (E4980AL Precision LCR Meter, Keysight Technologies). The four-probe method is used to directly measure a mutual impedance between coils [13]. Both amplitude and phase are acquired which represent resistive and inductive components. The effect of parasitic capacitance is suppressed by prior calibration and a commonly grounded screen placed in the outer perimeter of the sensors.

The two-coil system in Fig. 2 is extended into multi-channel measurements setup (Fig. 3) via computer-controlled data acquisition (DAQ970A Data Acquisition System, Keysight Technologies) and multiplexer (DAQM901A 20 Channel Multiplexer Module, Keysight Technologies) providing a projection system for the tomographic purpose. The setup is capable of scanning up to 28 –the combination of 8 coils taken 2 (a pair) at a time without repetition– independent rotational measurements; each of which acquires impedance values over frequency scope from 20 Hz to 300 kHz.

The direct induction effect is eliminated by taking amplitude ratio and phase difference of measurement with an object to a free-space measurement. Fig. 4 depicts the reference measurements for seven basic coil pairings.

B. Magnetic Induction Tomography

Mutual inductance tomography, also known in terms of magnetic induction tomography (MIT) or electromagnetic inductance tomography (EMT) [14], [15], works on several routines. Region of interest is excited by a magnetic field from the alternating current which flows through a coil. The field is then modified as a result of material distribution in the

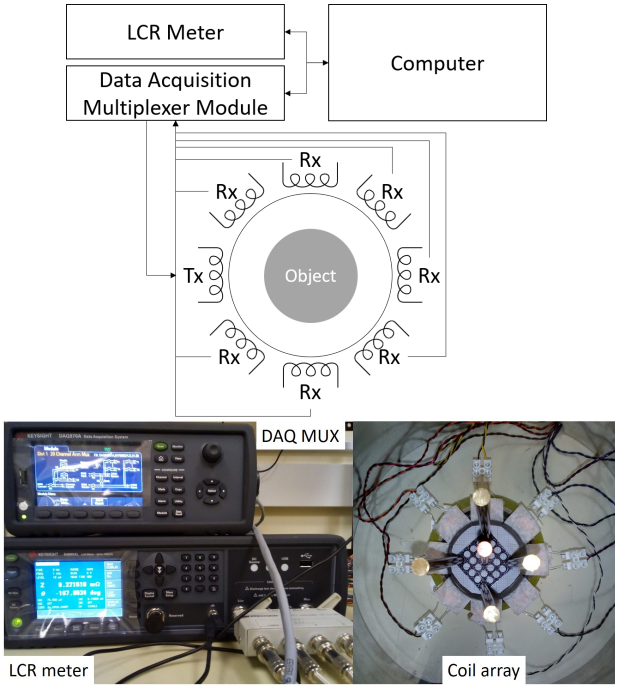

Fig. 3: Multi-Channels Setup for Tomographic Projection System.

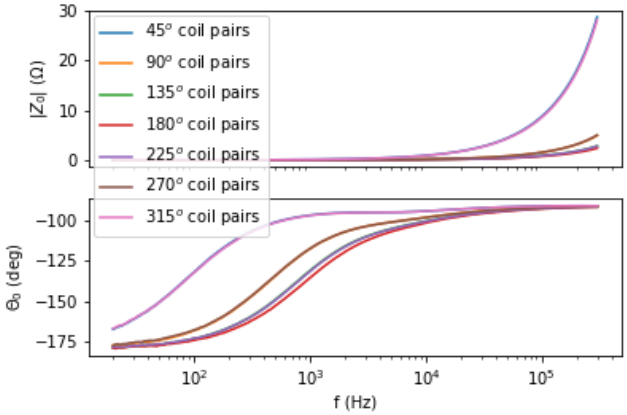

Fig. 4: Reference Measurement.

sensing space. These primary and secondary fields distributions are measured using an array of coils arranged (usually) circumventing the region. The boundary measurements can be reconstructed as an image using the inversion algorithm to map the electromagnetic properties in the sensing area. In addition to an image, another means of information such as parameters or profiles are also of interest. That information can be obtained directly from measurement or derived from reconstruction results.

C. Forward Modeling

Considering an imaging system where conductivity σ is sought, a formulation using magnetic vector potential $\mathbf{A}$ in the conductive region involves the gradient of electric scalar potential [16],

$$\nabla \times \left(\frac{1}{\mu} \times A\right) + j\omega\sigma A = J_s \tag{3}$$

where μ is permeability, ω is angular frequency, and $\mathbf{J_s}$ is source's current density.

A linear approximation can be applied only for a small perturbation on pixel value, and a linear response is assumed between the change in pixel value and the change in mutual inductance being measured between coil pairs. Supposed that there are k pixel each has a value of p_i representing electromagnetic property required from a pixel, then pixel values can be arranged to be a vector $\mathbf{P}$. Likewise, if there are n measured coil pairs each with the measured mutual inductance of m_j, then the measured values can be arranged into vector $\mathbf{M}$. Small change in $\mathbf{M}$ ($\Delta\mathbf{M}$) with change in $\mathbf{P}$ ($\Delta\mathbf{P}$) may be linearly related through sensitivity matrix $\mathbf{S}$ [17],

$$\Delta M = S\Delta P \tag{4}$$

Therefore, $\mathbf{S}$ is Jacobian matrix in the system where:

$$\Delta P = \begin{bmatrix} \Delta P_1 \\ \vdots \\ \Delta P_i \\ \vdots \\ \Delta P_k \end{bmatrix}; \Delta M = \begin{bmatrix} \Delta M_1 \\ \vdots \\ \Delta M_j \\ \vdots \\ \Delta M_n \end{bmatrix}; S = \begin{bmatrix} \frac{\partial m_1}{\partial p_1} & \cdots & \frac{\partial m_1}{\partial p_k} \\ \vdots & \ddots & \vdots \\ \frac{\partial m_n}{\partial p_1} & \cdots & \frac{\partial m_n}{\partial p_k} \end{bmatrix} \tag{5}$$

Due to signal's change is relative to empty (air) background, $\Delta\mathbf{P}$ and $\Delta\mathbf{M}$ are simply notated as $\mathbf{P}$ and $\mathbf{M}$ respectively. This coefficient $\mathbf{S}$ can be obtained experimentally by scanning small test object as a perturbation in the sensing space and measuring the response on every coil pairs accordingly. However, the common approach is to calculate $\frac{\partial m_j}{\partial p_i}$ using finite element modelling or vector field solution.

Mutual impedance changes (ΔZ) between transmitter and receiver coils affected by an object is derived. Taking into account the equation described in [18], [19], Lorentz reciprocity relation is considered and a generalised formula applies for coil pairs [20],

$$\begin{aligned} \Delta Z &= Z_b - Z_a \\ &= \frac{1}{I^2}\int_v j\omega(\mu_b - \mu_a)H_a \cdot H_b \\ &\quad -(\sigma_b + j\omega\varepsilon_b - \sigma_a - j\omega_a)E_a \cdot E_b dv \end{aligned} \tag{6}$$

where Z_a is the mutual impedance between coil pairs when properties of the medium are $(\mu_a, \sigma_a, \varepsilon_a)$. One of the coils is excited by a current I with angular frequency ω generating magnetic and electric fields H_a and E_a respectively. Z_b is the mutual impedance when properties of the medium are $(\mu_b, \sigma_b, \varepsilon_b)$. Identically, the other coil is excited by a current I with angular frequency ω generating magnetic and electric fields H_b and E_b respectively. The region v covers the medium (and object) under inspection.

In the interest of observing only a conductive object, the permeability change is neglected. Furthermore, as the reference measurement is air background, both conductivity σ_a and permittivity ε_a are negligible as well. Thus, (6) is simplified,

$$\Delta Z = -\frac{1}{I^2}\int_v (\sigma_b + j\omega\varepsilon_b)E_a \cdot E_b dv \tag{7}$$

As an attempt to reduce the coupling capacitance between coils and object, the sensing system is designed in such a way that the electric field generated by coils is eliminated. Consequently, for background condition $\nabla V \approx 0$, the electric field becomes,

$$E_a \approx -\frac{\partial A_a}{\partial t} = -j\omega A_a \tag{8}$$

whereas the current density in the object is,

$$J_b = (\sigma_b + j\omega\varepsilon_b)E_b \tag{9}$$

putting altogether (7), (8), and (9),

$$\begin{aligned}\Delta Z &\approx \frac{j\omega}{I^2}\int_v A_a \cdot E_b(\sigma_b + j\omega\varepsilon_b)dv \\ &= \frac{j\omega}{I^2}\int_v A_a \cdot J_b dv\end{aligned} \tag{10}$$

Therefore, an approximation for the system that observes complex conductivity changes related to the measurement of mutual impedance can be obtained as a discrete coefficient,

$$S = \frac{\Delta Z}{\Delta(\sigma + j\omega\varepsilon)} \tag{11}$$

Examples of sensitivity matrix derivation for some electromagnetic problems have been reported in [21] [22] [23] [24] [25].

Given a measurement apparatus that provides the change of mutual impedance δZ for a coil pair (i, j), the sensitivity S of that quantity due to the change of conductivity $\delta\sigma$ in the region of interest can be calculated,

$$S = \frac{\partial Z_{ij}}{\partial \sigma} = -\frac{\omega^2}{I_i I_j}\int A_i A_j \tag{12}$$

where A_i and A_j are field when coil i is excited by a current I_i and field when coil j is excited by current I_j respectively. The overall sensitivity is obtained by integration over discretization following the above.

D. Inverse Solving

The linear case has an inevitable limitation. Nevertheless, this method gives a rough qualitative image which indicates material distribution. The inversion determines P from the measurement of M. However, the sensitivity matrix S cannot be inverted in an obvious fashion. The Moore-Penrose generalised inverse $S^{\dagger}$ may be chosen [17],

$$S^{\dagger} = (S^T \cdot S)^{-1} \cdot S^T \tag{13}$$

where $P = S^{\dagger}M$ is least-square solution for $M = SP$, i.e. $min\|M - S \cdot P\|^2$. Mostly, the applications demand a large number of k than the number of measurements n. This makes the problem ill-posed, and computation of $(S^T \cdot S)^{-1}$ or $(S \cdot S^T)^{-1}$ has a numerical error. Thus, regularisation is required to minimise least square error as well as penalise large value in P,

$$min\{\|M - S \cdot P\|^2 + \alpha^2\|P\|^2\} \tag{14}$$

α^2 compromise between matching the data and controlling solution. The choice of α^2 represents the level of a priori knowledge related to the solution. Tikhonov regularisation is commonly used,

$$P = (S^T \cdot S + \alpha^2 I)^{-1} S^T M \tag{15}$$

The origin of this method can be traced from [26]. The inversion process to recover a conductivity distribution $\mathbf{K}$ in the sensing area from mutual impedance measurements $\mathbf{Z}$ is implemented as,

$$K \approx (S^T S + \lambda R)^{-1} S^T Z \tag{16}$$

where R and λ are the regularisation matrix and regularisation parameter respectively. This problem is rather a wide topic, thus ill-posed nature which needs to be addressed properly and other constraints related to regularisation, etc. are beyond the scope of this report. The single-step algorithm used in this work was described in [27] and proven for metallic imaging as reported in [28].

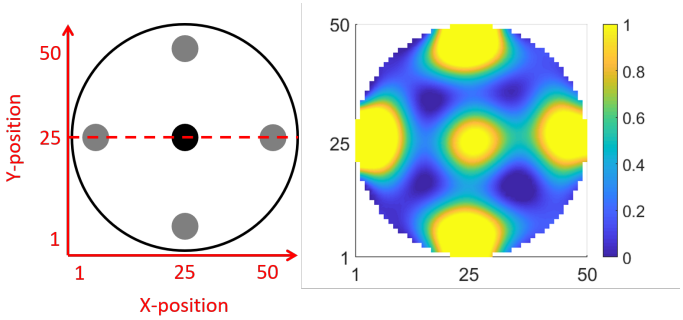

Fig. 5: Spatial Arrangement of Objects in the Sensing Region; and Example of MIT Image from Experiment with Five Metal Rods.

An example of MIT image reconstructed by aforementioned technique is shown in Fig. 5 (normalised value). The spatial region is divided into 50x50 pixel with effective circular area of 1976 pixels. Experimentally seen in Fig. 3, five metal samples are placed in the sensing space (d_{sample} = 6.25 mm; D_{space} = 60 mm), four of them (grey) have lower conductivity (σ = 16 MS/m) than an object in the middle (black, σ = 58 MS/m). As expected in soft-field tomography, region near the sensors poses a higher sensitivity compared to central region, and reflected on the resulting image.

Single-frequency measurement at 10 kHz (averaging ten datasets) is taken. This example is intended to show an overview of spatial (cross-section) image. In the subsequent spectral imaging, where reconstruction is being done for each frequency separately, the pixel values from $X_{position}$ = 1 to $X_{position}$ = 50, across $Y_{position}$ = 25 plane are evaluated

(indicated by dashed red-line). This constitutes spatial 'position' axis (vertical) against frequency axis (horizontal) in the 'surface plot' of the spectrum.

III. Spectroscopy

A. Mutual Impedance on Conductivity Level

Mutual impedance spectrum against air background measured from 20 Hz to 300 kHz (200 data points in logarithmic fashion) is shown in Fig. 6. Different samples with different conductivity produce sigmoid pattern where the inclination shifts to the left as conductivity increases.

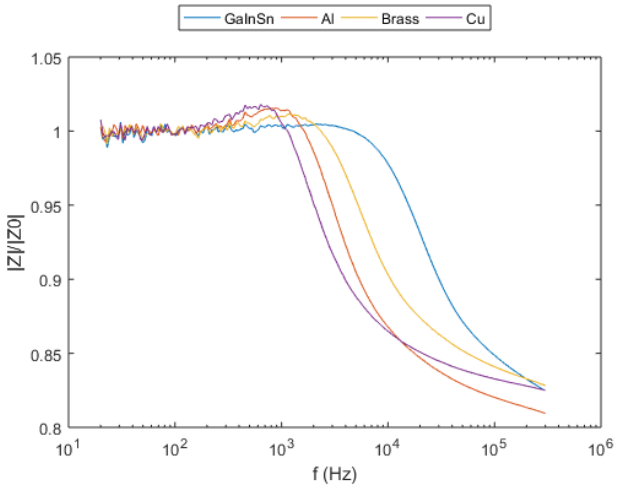

Fig. 6: Mutual Impedance Spectrum Conductive Samples.

Phase spectrum against air background is similarly swept in the frequency range (Fig. 7). Different samples with different conductivity produce bell pattern where the extreme valley shifts to the left as conductivity increases.

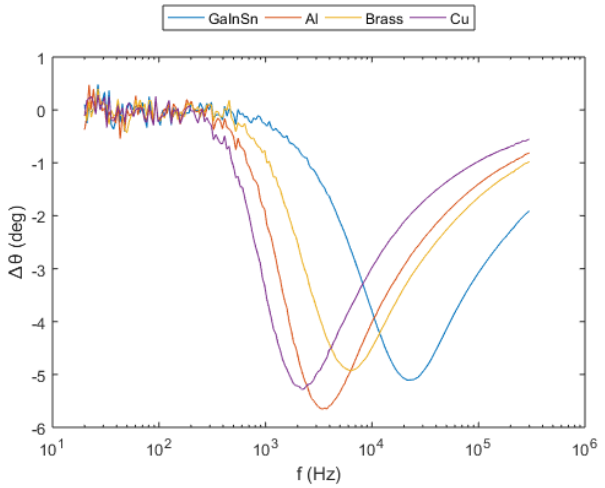

Fig. 7: Phase Spectrum Conductive Samples.

Both plots are produced from opposite coil measurement (setup Fig. 2) and consistent with modelling result (Fig. 1), taking into account a variation of conductivity values listed in Table I.

TABLE I: Conductivity of Tested Objects

Sample	σ (S/m)
Liquid GaInSn	0.32×10^7
Brass	1.61×10^7
Aluminum	2.63×10^7
Copper	5.84×10^7

Conductive samples are commercially available and comply with their standards and specifications, i.e. Ga–In–Sn eutectic alloy [29], brass rod (BS2874/CZ121M (1986); BS EN 12164/CW614N), aluminum (Al) rod (BS1474 HE30 TF (1987); BSEN 754-5 608 2T6), and copper (Cu) rod (BS2874/C101 (1986); BS EN 12164 CW 004A).

B. Mutual Impedance on Conductive Structure

The similar setup in Subsection III-A is implemented for three different conductive structures. Plastic (PLA) containers are prepared to hold liquid metal GaInSn in full, annular (50% area is hollowed in the centre), and bubbly (three voids each occupies 25% area distributed inline axially).

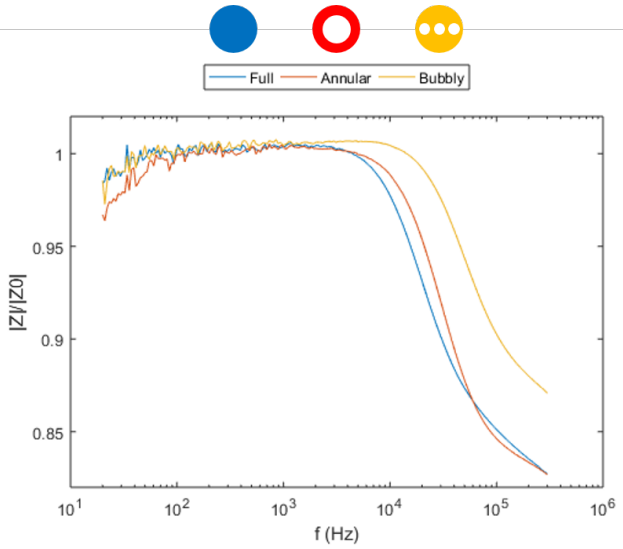

Fig. 8: Mutual Impedance Spectrum Conductive Structures.

Fig. 8 shows that the same material with different structures produces a sigmoid pattern. The curves for full and annular condition are close to each other and having intersection point at a certain frequency. Meanwhile, for bubbly case, the tendency in the curve is as though there was a decrease in conductivity, and the asymptote has a higher value.

Phase spectrum is shown in Fig. 9. Same material with different structures produces a bell pattern. The extreme valleys shift as though there was a decrease in conductivity level. The position of the valleys in y-axis also changes, while annular structure goes lower; bubbly structure goes higher.

C. Spectral Imaging of Mutual Impedance

Mutual impedance and phase spectrum measurements are collected for seven coil-pairs in a circular array consisting of

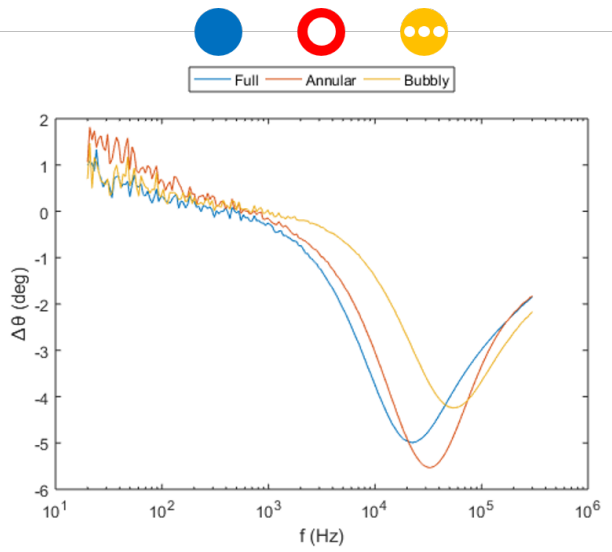

Fig. 9: Phase Spectrum Conductive Structures.

eight coils. The coil array is arranged enclosing the object in the sensing area (see Fig. 3). For a cylindrical object, full tomographic sensing is obtained by virtually rotating the coil array 45^o counter-clockwise in each step. Therefore, a sufficient number of independent measurements are acquired to be reconstructed as an image for every frequency data.

The images are reconstructed using the technique described in Subsection II-D. Simply, single-step reconstruction with neighbouring matrix and regularisation parameter of order 10^{-12} are used in this work. Resulting images are then piled to construct a whole spectral image. In this way, the horizontal direction of the image represents frequency; whereas vertical direction is spatial location. An example of aluminum rod half-inch of diameter produces mutual impedance and phase spectrum as shown in Fig. 10 and Fig. 11 respectively. Surface plot (top) in the figures is the spectral image, while semi-logarithmic plot (bottom part) is the associated measurement data. Each line plots measurement between transmitter-receiver coils paired to a certain degree. Both surface and semi-log plots share the same frequency axis.

Mutual impedance for seven coil-pairs gives familiar sigmoid patterns where inclinations lie on certain frequency indicating conductivity characteristics found in measurement (see Subsection III-A). The amplitude spectral reconstruction shows image patterns (centre area at pos=25 where the object is placed) starting from a high-contrast value (at low frequency) and finishing with low-contrast value (at high frequency). Similarly, phase change for seven coil-pairs produces bell shapes where extrema occur on specific frequency from which conductivity level can be inferred. The phase spectral image depicts high-contrast value (at the beginning), then down to low-contrast value (midway), and end-up back with high-contrast value. In other words, there is a gradient change of images along with the frequencies. Note that all colormap scales/values are qualitative resulting from the inverse calculation (affected by parameters and Jacobian), hence the interpretation of which is another subject for the follow-up

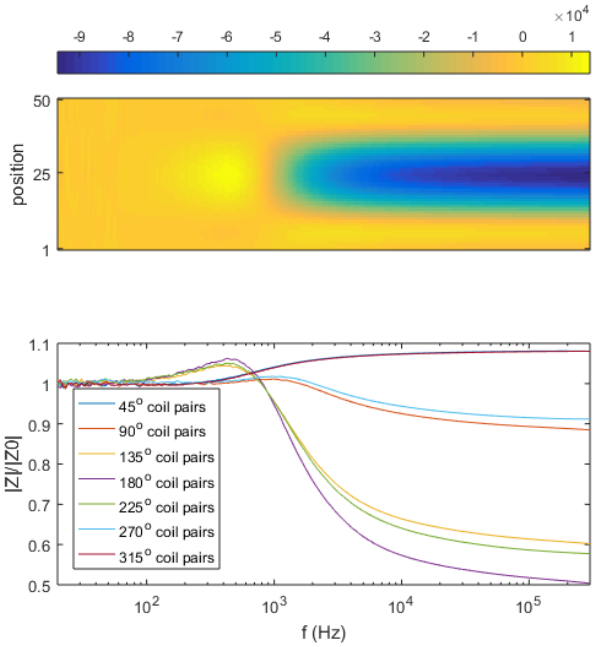

Fig. 10: Mutual Impedance Spectrum Aluminum Rod 0.5in. Top: Spectral Image at Spatial Position Against Frequency. Bottom: Measurement plot. Both Share Common Horizontal Frequency Axis.

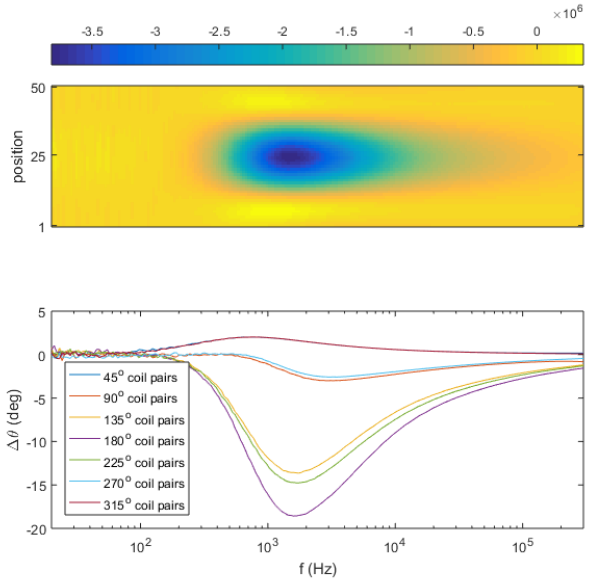

Fig. 11: Phase Spectrum Aluminum Rod 0.5in. Top: Spectral Image at Spatial Position Against Frequency. Bottom: Measurement Plot. Both Share Common Horizontal Frequency Axis.

work.

In order to obviously show the fingerprints of each object's circumstances, mutual impedance spectrums are compiled in a single plot. They are arranged as follows: four individual images of four different samples are taken, with the sample with the highest conductivity at the top and the sample with the lowest conductivity at the bottom ($\sigma_{Cu} > \sigma_{Al} > \sigma_{Brass} > \sigma_{GaInSn}$). In the measurement, the object is located at the central location (pos = 25) in the sensing space. All plots share the same frequency (horizontal) axis. Fig. 12 and Fig. 13 show shifting colour contrast to lower frequency as conductivity level increases.

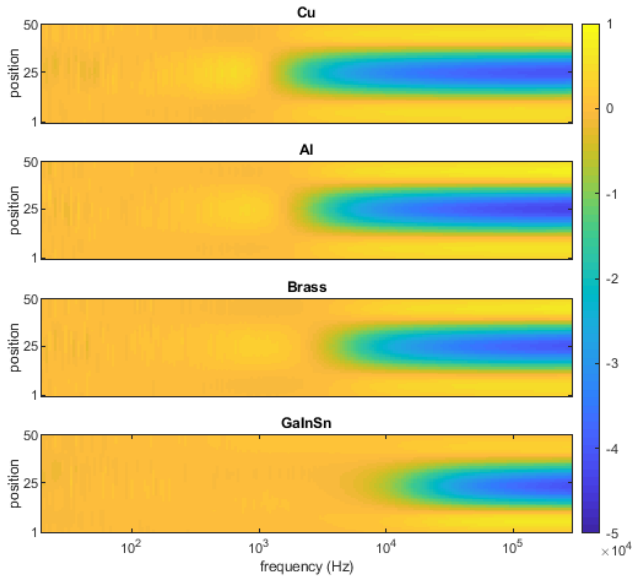

Fig. 12: Mutual Impedance Spectrum Imaging Conductivity. Individual Samples (d = 0.25in) are Exposed. Each Plot (Top-to-Bottom): Cu (σ = 58.4 MS/m), Al (σ = 26.3 MS/m), Brass (σ = 16.1 MS/m), GaInSn (σ = 3.2 MS/m). All Plots Share Common Horizontal Frequency Axis.

IV. Application

The aforementioned techniques are applied in the following two scenarios. Subsection IV-A explains a case of liquid metal inclusion which is of interest in the steel casting process. For the conventional method, field distribution in the case of complex structure is less definite [30]. Another describes contactless temperature measurement utilising the conductive body as an agent through which the magnetic induction method is capable of sensing the temperature change and mapping its distribution according to conductivity variation. Electromagnetic methods for thermography are well-known such as infrared and magnetic resonance [31]. While an electrical resistance device and capacitance thermometry offer invasive technique, the inductive method provides a non-contact solution.

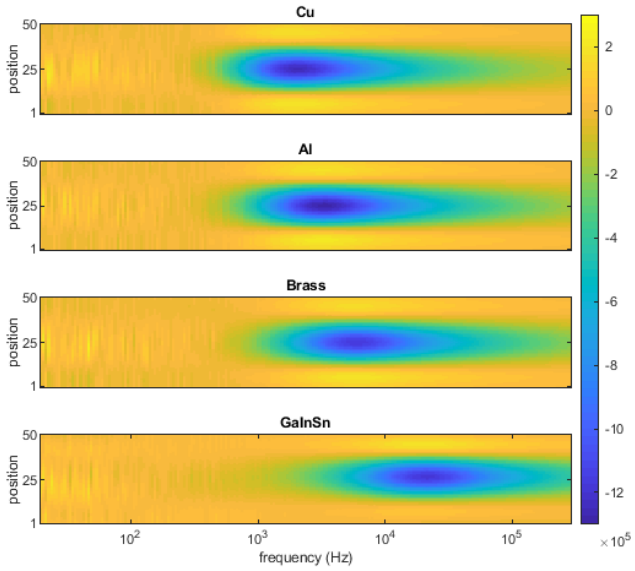

Fig. 13: Phase Spectrum Imaging Conductivity. Individual Samples (d = 0.25in) are Exposed. Each Plot (Top-to-Bottom): Cu (σ = 58.4 MS/m), Al (σ = 26.3 MS/m), Brass (σ = 16.1 MS/m), GaInSn (σ = 3.2 MS/m). All Plots Share Common Horizontal Frequency Axis.

A. Inclusion in Liquid Metal

Experiments are conducted using liquid metal (Ga-In-Sn) as a conductive sample that is detectable by multi-frequency impedance and phase measurements. Fig. 14 shows the measurement setup. The coil arrays are made from eight air-cored solenoids (8 mm height, 25 mm outer diameter, 10 mm inner diameter, 23 AWG wire, 100 turns) encircling 60 mm diameter of the sensing area. A grounded conductive screening sheet (150 mm height, 250 mm diameter) is placed around the perimeter to reduce the ambient noise.

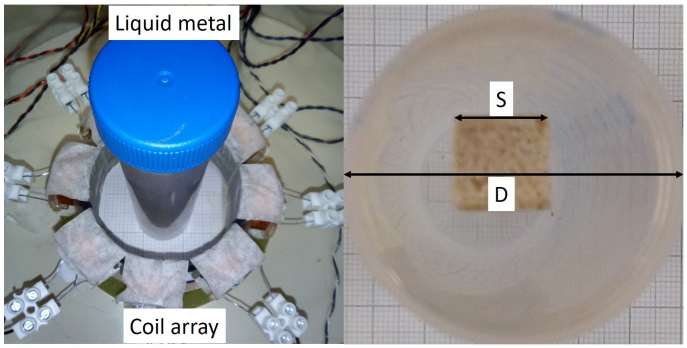

Fig. 14: Experiment Setup for Liquid Metal Inclusion.

Firstly, impedance and phase are measured for 1 inch of diameter (D) plastic tube fully-filled with the liquid metal and plotted against air background. The plot is then considered as the reference for subsequent measurements where a non-conductive inclusion is introduced in the liquid metal body. It is assumed that the insertion of non-conductive material

will disrupt the eddy current distribution which occurs freely on the full liquid metal circumstance. Therefore, the overall conductivity of the body is expected to change and a shift should be apparent around extreme points in the mutual impedance and phase graphs.

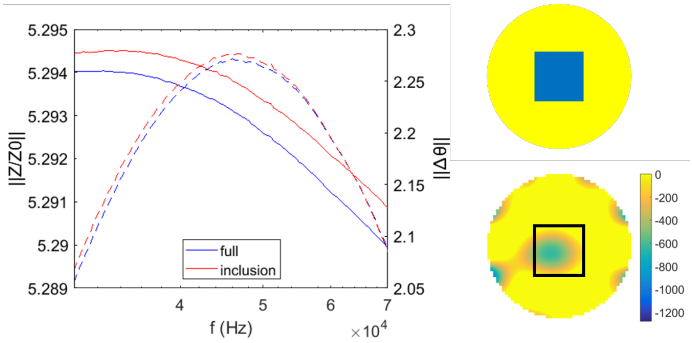

Fig. 15: Mutual Impedance Liquid Metal Inclusion. Left: impedance plot (—) on left axis; phase plot (- -) on right axis. Right: inclusion true distribution (top) and reconstructed image (bottom).

A squared wood (balsa) with size of 9.5 mm (S) is immersed in the test. It can be seen from graph in Fig. 15 (left) that an inclusion will shift the plot. Since the inclusion's precise location is unknown due to opacity of the liquid metal, all mutual combination between 8-coil arrays are measured, and norm values are taken. Note that this method does not necessarily require low-frequency measurement to penetrate conductive samples in order to detect an inclusion inside them. As a result, the frequency region can be contained into a range of interests based on the fundamental plot for liquid metal Ga-In-Sn.

Cross-section true and constructed images are shown in Fig. 15 (right). Image reconstruction produces good consistency along the spectrum of interest. Therefore, mean values are applied here to illustrate inclusion's image (non-conductive) and its location (black line border) inside the liquid metal. Quantitative analysis in spatial imaging is used to evaluate the liquid metal correlation coefficient (0.63) and area error of 0.16 which are in an acceptable agreement with the true distribution.

B. Temperature Sensing

Certain phenomena are dependent on temperature, hence exploitable for instrumentation. Making use of the renowned physical properties that is the resistivity of a material is a function of its temperature, multi-frequency mutual impedance and phase can also be employed for indirectly sensing the change in the temperature of a medium surrounding a conductive body. This is applicable when the conductive body and the medium exchange heat, unisolated towards one another.

The experiment setup is shown in Fig. 16, with the same coil array and sensing space as described in Subsection IV-A. A metal sample (Al rod) is prepared in a container filled with water, in the centre of coils. Mutual impedance and phase between coil combinations are measured. Water temperature

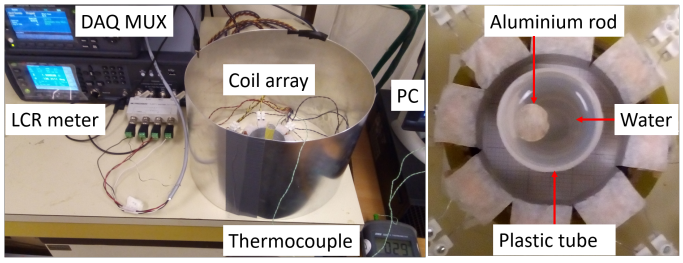

Fig. 16: Experiment Setup for Temperature Sensing.

is varied from cold to hot condition and measurements are taken in cycles, keeping the object intact in the sensing region. The temperature is tested using a thermocouple (CHY 500 K) before and after each mutual impedance measurements cycle in order to avoid the influence of magnetic fields on the thermocouple probe and vice versa. Multi-frequency graphs are plotted (norm, against air background) showing distinct shifts for different temperatures in Fig. 17 (left). Note that the plot composes from two setups, i.e. cold (up to 20 ^oC) and hot (from 25 ^oC). Having different background measurements and the relative position of the metal sample in the water medium, a slight change in trend is anticipated.

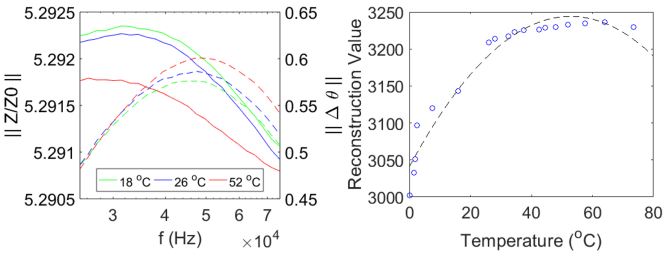

Fig. 17: Mutual Impedance Temperature Sensing. Left: impedance plot (—) on left axis; phase plot (- -) on right axis. Right: reconstruction value against temperature.

Both impedance and phase plots indicate the change of the sample's conductivity confirming the change of water's temperature. The frequency range where extreme values and pronounce shifts lie can be taken as measurement reference for more complex detection scheme.

The data are then converted into imaging domain for assessing the correlation between reconstruction value and temperature change, giving the trend shown in Fig. 17 (right). This can be derived as:

$$y = p_1 x^2 + p_2 x + p_3 \tag{17}$$

where the quadratic fit coefficients are: p_1 = -0.072838, p_2 = 7.6959, p_3 = 3040.8; whereas norm of residuals = 72.736. The reconstruction values are calculated from the mean of unique numbers across the image sections. Equation (17) is also affected by regularisation parameters of the image reconstruction, thus can be used as calibration function.

A complete two-dimensional tomographic heat mapping is attempted through an experiment using the similar metal samples in different locations with some temperature variations

between them. The setup in Fig. 18 (left) shows two half-inch aluminum rods placed in sensing space. An object (obj-1) next to coil-1 was heated beforehand; meanwhile, the opposite obj-2 (near coil-5) is at room temperature.

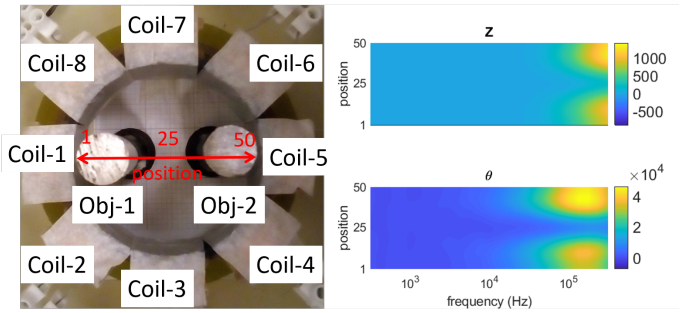

Fig. 18: Conductive Objects Distribution and The Impedance-Phase Spectrum. Left: Spatial Location in the Sensing Space [1 50]. Right: Surface Plot of Position (Vertical Axis) vs Frequency (Horizontal Axis).

The reconstructed impedance and phase spectrum is shown in Fig. 18 (right). Three decades of frequency are swept (in log) for respective measurements and put into (a shared) horizontal axis. The location in the sensing region (along the red-line [1–50]) is allocated to the vertical axis. It can be seen that the images become more pronounced at higher frequencies, having different colormap level which indicates the temperature difference.

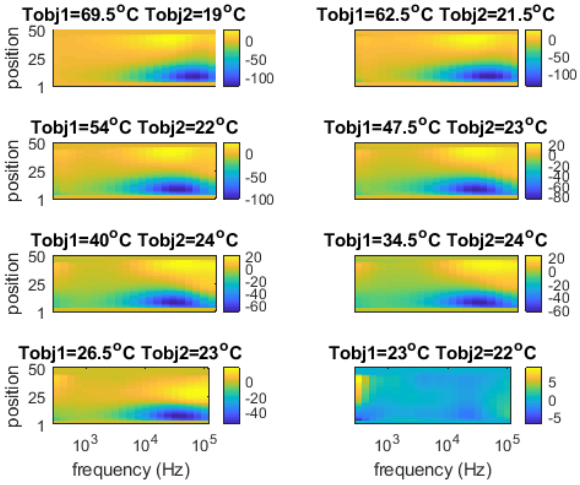

Fig. 19: Spatial and Spectral Color Map.

Referring to the spectral information from two conductive objects in different circumstances (position and temperature), a subsequent test is conducted keeping track of the temperature of both objects. Once both object reach room temperature, the respective measurement data are treated as reference data (in addition to air background measurement). Phase spectrum for several conditions are given in Fig. 19. It depicts the distribution of conductive object in different temperatures relative to a condition at room temperature. There are 25 frequency points between 300 Hz – 300 kHz in logarithmic space. The arrangement of the experimental setup and its respective surface plot are similar to that in Fig. 18. Plots on the right-column share the same vertical 'position' axis with those on the left-side; and all share the common horizontal 'frequency' axis of the bottom-row plots. Position = 1 represents location near coil-1 (where object-1 is placed having temperature of T_{obj1}); whereas position = 50 is location near coil-5 (where object-2 is placed having temperature of T_{obj2}). There are distinct illustrations (scaled individually) of temperature change related to conductivity change of the objects due to heating. A larger temperature difference between samples (reconstructed area) produces a wider color-scale range respectively.

Quantitative analysis taking the mean value of reconstructed heat map along the evaluated spectrum provides a reasonable trend in Fig. 20. Temperature difference ($\Delta T = T_{obj1} - T_{obj2}$) of 1 ^oC gives the value of 0.152; meanwhile at the other end, value of 13.65 is obtained for 41 ^oC of difference in temperature.

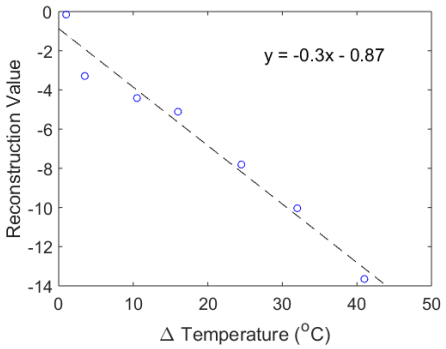

Fig. 20: Reonstruction Value vs Temperature Difference in Heat Map.

Another test case is the detection of pipe's temperature in which a heated fluid is contained (Fig. 21). A copper pipe (42 mm outer diameter, 40 mm inner diameter) is placed in the sensing region. It is filled with water whose temperature is varied. Mutual impedance measurements are taken in cycles while monitoring the water temperature.

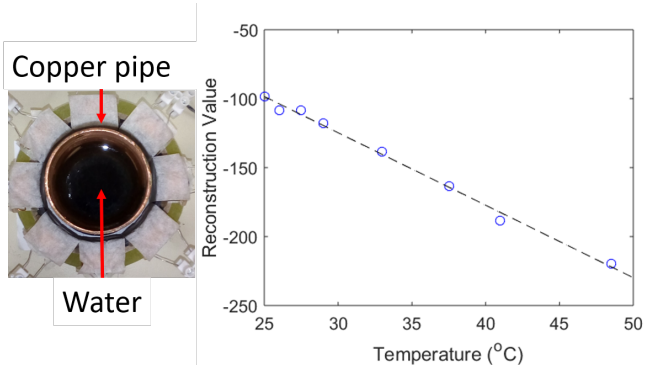

Fig. 21: Experiment Setup for Temperature Sensing in Pipe.

Phase data along the spectrum of 100 Hz – 100 kHz are reconstructed and evaluated according to water's temperature, using room temperature state as reference. Imaging value is

correlated with thermocouple reading as shown in Fig. 21 (right) and fitted in the following:

$$y = p_1 x + p_2 \tag{18}$$

where the linear coefficients are: p_1 = -5.2561, p_2 = -32.972; whereas norm of residuals = 8.7962. For this particular situation, heating of the coil is considered due to a small gap between the pipe's surface and the coil array. Experiment cycles are timely conditioned to allow stable heat distribution. In terms of image reconstruction, the area near to coil has a higher sensitivity and should be carefully evaluated. Nevertheless, (18) provides an acceptable trend.

The quadratic polynomial temperature fit of Fig. 17 is to be used for relatively wide temperature measurement range (in this case 0–80 ^oC) inside an object (assumed due to some physical effects in the aluminum sample); while the linear fit would be properly applied for temperature distribution (heat mapping) or a relatively narrow variation of surface temperature. Still, particular measurement situations are proven.

V. Discussion

Measurement techniques for liquid metal were reviewed in [32]. Inclusion (in the form of gas bubbles) can be observed using ultrasound transit-time (UTT), contactless inductive detection, and X-ray imaging. The UTT can quantify gas bubble with diameter 5 – 7 mm without producing an image. However, any impurity or unclean medium will hinder the sound transmission, hence its detection capability. On the other hand, high-resolution X-ray can recover the gas bubbles image down to about 1 mm with a maximum thickness of the fluid layer of about 15 mm. This limitation arises due to the ray is highly attenuated through a conductive medium. Therefore, given an adequate penetration depth, the inductive method is favourable for industrial implementation. This work offers a non-invasive and non-intrusive measurement technique to investigate non-conductive inclusion inside a conductive body. It paves way for potential applications on conductvity level or metal classification, and could be extended to gas bubble content determination in liquid metal flow.

State-of-the-art of contactless technique for measuring and determining temperature distribution in industrial application is infrared thermal imaging [33]. Commercial thermal cameras are available with typical sensitivity about 0.05 ^oC (within the range -40 ^oC to 550 ^oC), a specified accuracy of ± 5 ^oC, and spatial resolution approximately 1 mm/pixel (320×240 elements at 1 m object to camera distance) [34]. However, infrared thermography (IRT) requires optical access to the object's surface. On the other hand, the main advantage of the proposed method is that it can be used against an opaque structure. Although the sensitivity is limited to 1 ^oC (based on the test between 0 to 80 ^oC measured by thermocouple with resolution 0.1 ^oC and accuracy ± 1 ^oC), the spatial resolution can reach about 1.2 mm/pixel (50×50 elements enclosing the object). Note that both techniques still need calibration, parameters setting, and (sometimes for IRT) inversion process which are comparatively not straightforward. Utilising a difference imaging, this noninvasive inductive temperature sensing is suitable for condition monitoring (temperature uniformity) in, for instances, pipe under-cladding, metal implant, or buried conductive materials.

The change of conductivity due to the change of temperature in materials is an established principle. This paper discloses some technical solutions using procedures which have been shown in the experiments. The use of magnetic induction spectroscopy and its imaging results for accomplishing such task provides rich information. However, some disadvantages should be anticipated. Tests have been conducted for relatively low-ranged temperature estimation, and the resolution would be affected by imaging quality from which the temperature values are extracted. Soft-field tomography imaging such as electromagnetic tomography is an ill-posed problem, hence the reconstruction is challenging. Besides spatial constraint, the temporal ability of the conductivity reconstruction should be considered for catching the continuous transient change in temperature variability for typical industrial settings. In addition, more uncertainties occur compared with 1-dimensional measurement methods. The proposed technique has advantages of a remote measurement, enhanced with temperature mapping without the need to either physical or optical access required by conventional means. Albeit limited, this method would still find suitable applications once the aforementioned aspects are accounted.

VI. Conclusion

Mutual impedance and phase spectra have been observed for metal objects with different conductivity level using MIT. Depicted in a spectroscopic fashion, perplexity of electromagnetic tomography reconstruction is reposed when the imaging spectrum pronounces substantial information about the physical properties of an object. A distinct shift in the amplitude, accompanied by gradient location in the phase are valuable insight upon which more sophisticated work can be built. Some foreseeable implementations are phase distribution of a conductive substance in a concealed vessel, e.g. steel flow in continuous casting, as well as temperature-dependent conductivity mapping inside a physically and/or optically inaccessible region. The magnetic induction sensing system is inherently immune to surrounding contamination, robust in construction, and cost-effective for industrial deployment. For the first time we demonstrated it is possible to derive a temperature and temperature distribution of a known metal using spectroscopic eddy current data. This will open up a new type of thermal mapping sensing devices for many industrial and other applications that are need of fully noninvasive thermal mapping.

Acknowledgment

This project has received funding from the European Union's Horizon 2020 research and innovation programme under the Marie Skłodowska-Curie grant agreement No 764902. The authors would like to thank G. P. Dingley and D. J. Chapman for their help in measurement setup. We would also like to thank anonymous reviewers for their comments and suggestions that improved the manuscript.

REFERENCES

[1] J. R. Wait, "A conducting permeable sphere in the presence of a coil carrying an oscillating current," *Canadian Journal of Physics*, vol. 31, no. 4, pp. 670–678, 1953.

[2] ——, "Some solutions for electromagnetic problems involving spheroidal, spherical and cylindrical bodies," *J. Res. Nat. Bur. Stand. B*, vol. 64, pp. 15–32, 1960.

[3] I. J. Won, D. A. Keiswetter, and T. H. Bell, "Electromagnetic induction spectroscopy for clearing landmines," *IEEE Transactions on Geoscience and Remote Sensing*, vol. 39, no. 4, pp. 703–709, April 2001.

[4] Haoping Huang and I. J. Won, "Automated identification of buried landmines using normalized electromagnetic induction spectroscopy," *IEEE Transactions on Geoscience and Remote Sensing*, vol. 41, no. 3, pp. 640–651, March 2003.

[5] O. A. Abdel-Rehim, J. L. Davidson, L. A. Marsh, M. D. O'Toole, and A. J. Peyton, "Magnetic polarizability tensor spectroscopy for low metal anti-personnel mine surrogates," *IEEE Sensors Journal*, vol. 16, no. 10, pp. 3775–3783, May 2016.

[6] M. D. O'Toole, N. Karimian, and A. J. Peyton, "Classification of nonferrous metals using magnetic induction spectroscopy," *IEEE Transactions on Industrial Informatics*, vol. 14, no. 8, pp. 3477–3485, Aug 2018.

[7] Wuliang Yin, S. J. Dickinson, and A. J. Peyton, "Imaging the continuous conductivity profile within layered metal structures using inductance spectroscopy," *IEEE Sensors Journal*, vol. 5, no. 2, pp. 161–166, April 2005.

[8] T. Wondrak, U. Hampel, M. Ratajczak, I. Glavinic, F. Stefani, S. Eckert, D. van der Plas, P. Pennerstorfer, I. Muttakin, M. Soleimani, S. Abouelazayem, J. Hlava, A. Blishchik, and S. Kenjeres, "Real-time control of the mould flow in a model of continuous casting in frame of the TOMOCON project," *IOP Conference Series: Materials Science and Engineering*, vol. 424, p. 012003, oct 2018.

[9] R. Binns, A. R. A. Lyons, A. J. Peyton, and W. D. N. Pritchard, "Imaging molten steel flow profiles," *Measurement Science and Technology*, vol. 12, no. 8, pp. 1132–1138, aug 2001.

[10] M. Soleimani, F. Li, S. Spagnul, J. Palacios, J. I. Barbero, T. Gutiérrez, and A. Viotto, "In situ steel solidification imaging in continuous casting using magnetic induction tomography," *Measurement Science and Technology*, vol. 31, no. 6, p. 065401, mar 2020.

[11] D. Ross-Pinnock and P. G. Maropoulos, "Review of industrial temperature measurement technologies and research priorities for the thermal characterisation of the factories of the future," *Proceedings of the Institution of Mechanical Engineers, Part B: Journal of Engineering Manufacture*, vol. 230, no. 5, pp. 793–806, 2016.

[12] B. Dekdouk, W. Yin, C. Ktistis, D. W. Armitage, and A. J. Peyton, "A method to solve the forward problem in magnetic induction tomography based on the weakly coupled field approximation," *IEEE Transactions on Biomedical Engineering*, vol. 57, no. 4, pp. 914–921, April 2010.

[13] Z. Cui, Y. Chen, and H. Wang, "A dual-modality integrated sensor for electrical capacitance tomography and electromagnetic tomography," *IEEE Sensors Journal*, vol. 19, no. 21, pp. 10 016–10 026, Nov 2019.

[14] Z. Z. Yu, A. T. Peyton, M. S. Beck, W. F. Conway, and L. A. Xu, "Imaging system based on electromagnetic tomography (emt)," *Electronics Letters*, vol. 29, no. 7, pp. 625–626, April 1993.

[15] A. J. Peyton, Z. Z. Yu, G. Lyon, S. Al-Zeibak, J. Ferreira, J. Velez, F. Linhares, A. R. Borges, H. L. Xiong, N. H. Saunders, and M. S. Beck, "An overview of electromagnetic inductance tomography: description of three different systems," *Measurement Science and Technology*, vol. 7, no. 3, pp. 261–271, mar 1996.

[16] M. Soleimani, W. R. B. Lionheart, and A. J. Peyton, "Image reconstruction for high-contrast conductivity imaging in mutual induction tomography for industrial applications," *IEEE Transactions on Instrumentation and Measurement*, vol. 56, no. 5, pp. 2024–2032, Oct 2007.

[17] A. J. Peyton, "Electromagnetic induction tomography," in *Industrial Tomography: Systems and Applications*, M. Wang, Ed. Woodhead Publishing, 2015, pp. 61–107.

[18] J. R. Mortarelli, "A generalization of the geselowitz relationship useful in impedance plethysmographic field calculations," *IEEE Transactions on Biomedical Engineering*, vol. BME-27, no. 11, pp. 665–667, Nov 1980.

[19] B. A. Auld and J. C. Moulder, "Review of advances in quantitative eddy current nondestructive evaluation," *Journal of Nondestructive Evaluation*, vol. 18, no. 1, pp. 3–36, Mar 1999. [Online]. Available: https://doi.org/10.1023/A:1021898520626

[20] C. Ktistis, D. W. Armitage, and A. J. Peyton, "Calculation of the forward problem for absolute image reconstruction in MIT," *Physiological Measurement*, vol. 29, no. 6, pp. S455–S464, jun 2008.

[21] S. J. Norton and J. R. Bowler, "Theory of eddy current inversion," *Journal of Applied Physics*, vol. 73, no. 2, pp. 501–512, 1993.

[22] D. Dyck, D. Lowther, and E. Freeman, "A method of computing the sensitivity of electromagnetic quantities to changes in materials and sources," *IEEE Transactions on Magnetics*, vol. 30, no. 5, pp. 3415–3418, 1994.

[23] K. Hollaus, C. Magele, R. Merwa, and H. Scharfetter, "Fast calculation of the sensitivity matrix in magnetic induction tomography by tetrahedral edge finite elements and the reciprocity theorem," *Physiological measurement*, vol. 25, no. 1, p. 159, 2004.

[24] M. Soleimani and W. R. Lionheart, "Absolute conductivity reconstruction in magnetic induction tomography using a nonlinear method," *IEEE Transactions on medical imaging*, vol. 25, no. 12, pp. 1521–1530, 2006.

[25] W. Yin and A. J. Peyton, "Sensitivity formulation including velocity effects for electromagnetic induction systems," *IEEE Transactions on Magnetics*, vol. 46, no. 5, pp. 1172–1176, 2010.

[26] A. N. Tikhonov and V. I. Arsenin, *Solutions of ill-posed problems*. Winston, Washington, DC, 1977, vol. 14.

[27] H. Scharfetter, K. Hollaus, J. Rosell-Ferrer, and R. Merwa, "Single-step 3-d image reconstruction in magnetic induction tomography: Theoretical limits of spatial resolution and contrast to noise ratio," *Annals of Biomedical Engineering*, vol. 34, no. 11, pp. 1786–1798, Nov 2006. [Online]. Available: https://doi.org/10.1007/s10439-006-9177-6

[28] M. Soleimani, A. Adler, T. Dai, and A. J. Peyton, "Application of a single step temporal imaging of magnetic induction tomography for metal flow visualisation," *Insight - Non-Destructive Testing and Condition Monitoring*, vol. 50, no. 1, pp. 25–29, 2008.

[29] Y. Plevachuk, V. Sklyarchuk, S. Eckert, G. Gerbeth, and R. Novakovic, "Thermophysical Properties of the Liquid Ga–In–Sn Eutectic Alloy," *Journal of Chemical & Engineering Data*, vol. 59, no. 3, pp. 757–763, mar 2014. [Online]. Available: https://doi.org/10.1021/je400882q

[30] H. Tesfalem, A. J. Peyton, A. D. Fletcher, M. Brown, and B. Chapman, "Conductivity profiling of graphite moderator bricks from multi-frequency eddy current measurements," *IEEE Sensors Journal*, pp. 1–1, 2020.

[31] P. R. N. Childs, J. R. Greenwood, and C. A. Long, "Review of temperature measurement," *Review of Scientific Instruments*, vol. 71, no. 8, pp. 2959–2978, 2000. [Online]. Available: https://doi.org/10.1063/1.1305516

[32] M. Ratajczak, D. Hernández, T. Richter, D. Otte, D. Buchenau, N. Krauter, and T. Wondrak, "Measurement techniques for liquid metals," *IOP Conference Series: Materials Science and Engineering*, vol. 228, p. 012023, jul 2017.

[33] R. Alfredo Osornio-Rios, J. A. Antonino-Daviu, and R. de Jesus Romero-Troncoso, "Recent industrial applications of infrared thermography: A review," *IEEE Transactions on Industrial Informatics*, vol. 15, no. 2, pp. 615–625, 2019.

[34] S. Bagavathiappan, B. Lahiri, T. Saravanan, J. Philip, and T. Jayakumar, "Infrared thermography for condition monitoring – a review," *Infrared Physics & Technology*, vol. 60, pp. 35 – 55, 2013.

PLACE PHOTO HERE

Imamul Muttakin Biography text here.

Manuchehr Soleimani Biography text here.